Biomechanics and Modeling in Mechanobiology
https://doi.org/10.1007/s10237-025-01996-x

ORIGINAL PAPER

Patient-specific numerical simulation of compression therapy effects on interstitial fluid motion in lower limb lymphedema

Maha Reda[1] · **Stéphane Avril**[1]

Received: 14 April 2025 / Accepted: 12 July 2025

Abstract

Lymphedema is a chronic condition characterized by impaired lymphatic drainage, leading to fluid accumulation, swelling, and progressive tissue remodeling. Compression therapy is the primary treatment used to alleviate swelling and enhance fluid drainage, yet its precise impact on interstitial fluid dynamics remains to be understood. In this study, we developed a poroelastic computational model that simulates fluid flow and tissue deformation in the lower limb under different compression strategies and compression levels. A key feature of our work is the integration of patient-specific geometries, allowing for a more physiologically accurate representation of tissue mechanics and fluid redistribution. We simulated edema formation induced by venous insufficiency by increasing blood capillary pressure from a baseline of 10–80 mmHg, and we observed that interstitial fluid pressure (IFP) increased from a baseline value of 0 mmHg to 8 mmHg, highlighting the impact of vascular dysfunction on fluid accumulation. Simulating complete blockage of lymphatic capillaries resulted in even higher IFP values (40 mmHg) compared to models with functional lymphatics, where IFP remained around 8 mmHg for high capillary pressures, underscoring the critical role of lymphatic drainage. We further showed that an increase in tissue permeability increases gravity-driven fluid pooling, potentially exacerbating swelling in lymphedematous limbs. Additionally, we incorporated an interface pressure derived from Laplace's law to offer a more realistic estimation of IFP and volume changes, emphasizing its importance for refining compression models and optimizing treatment strategies. These findings contribute to a deeper understanding of compression therapy's role in interstitial fluid drainage and provide a foundation for improving patient-specific lymphedema management.

Keywords Lymphedema · Compression therapy · Interstitial fluid · Computational modeling · Patient-specific

1 Introduction

Lower limb lymphedema is a chronic and often debilitating condition characterized by the accumulation of interstitial fluid in the soft tissues of the lower extremities (Morgan et al. 2005). Generally, this fluid accumulation occurs due to a disruption in the lymphatic system which, under physiological conditions, acts as a drainage network that removes excess fluid from the tissues and prevents their swelling (Swartz 2001; Moore and Bertram 2018). The drainage mechanism relies primarily on passive flow induced by pressure gradients between the surrounding tissues and the lymphatic capillaries. In addition, the intrinsic contractions of the lymphangions serve as a pump that helps transport the fluid to the lymphatic nodes, where it is filtered before recirculating back into the veins. Lymphatic drainage in the lower limbs is challenged by gravitational forces, especially during prolonged standing positions. Hence, in addition to intrinsic contractions, extrinsic movements such as calf muscle contraction during physical activity, can further enhance the drainage mechanism by pushing the fluid through the vessels. The presence of lymphatic valves ensures a unidirectional flow inside the vessels and minimizes backflow. A delicate balance between these regulatory mechanisms helps maintaining a near atmospheric interstitial fluid pressure (IFP) and a constant volume of the lower limb (Brace 1981; Jamalian et al. 2017).

Lymphedema can manifest in two forms: primary and secondary. Primary lymphedema is a rare inherited genetic

✉ Stéphane Avril
avril@emse.fr

Maha Reda
maha.reda@emse.fr

[1] Mines Saint-Etienne, INSERM, U1059 Sainbiose, 42023 Saint-Etienne, France

disorder, while secondary lymphedema is an acquired condition with a higher prevalence in population (Brix et al. 2021). The onset of secondary lymphedema is multi-factorial. For instance, venous insufficiency, a condition characterized by dysfunctional venous valves, can lead to blood pooling inside the blood capillaries. This often results in an increased internal fluid pressure, leading to excessive fluid filtration from the blood capillaries, exceeding the drainage capacity of the lymphatic network and resulting in increased IFP in the tissues (Bunke et al. 2009). While this condition initially leads to edema due to increased capillary filtration, the sustained elevation in interstitial fluid volume can chronically challenge the transport capacity of the lymphatic system and contribute to the development of secondary lymphedema. Moreover, when the lymphatic vessels or nodes are compromised, the fluid cannot be adequately removed, leading to characteristic swelling and potential tissue damage. For example, the removal of lymph nodes during lymphadenectomy, often performed during cancer treatment, leads to drainage pathways obstruction, reducing the clearance capacity of the lymphatic system (Biglia et al. 2015).

Lymphedema is classified into four distinct stages according to disease severity, ranging from the initial, reversible stage characterized by mild swelling to the most advanced stage, where significant fibrosis and tissue hardening occur (Tassenoy et al. 2016). Once fibrosis occurs, tissues become stiffer, obstructing lymphatic vessels and impairing the pumping efficiency of the collecting lymphatics, which further contributes to limb swelling (Dayan et al. 2020). Nonetheless, early-stage lymphedema where swelling remains reversible, can often be managed using compression devices and bandages. Compression therapy aims to maintain pressure gradients in the tissue thereby enhancing lymphatic drainage (Cariati et al. 2012; Uzkeser et al. 2015; Partsch et al. 2010). By applying sustained pressure, compression helps limit swelling, reduce limb volume, and prevent disease progression to irreversible fibrotic stages. Compression devices vary significantly in design and functionality, ranging from static compression garments that apply uniform or pressure gradient along the leg to dynamic compression devices such as intermittent pneumatic pumps (Zaleska et al. 2014, 2015). Despite their extensive clinical use and their proven efficacy in reducing lymphedema, the interaction between compression devices and lymphatic drainage, as well as their impact on interstitial fluid dynamics, remain poorly understood.

In recent decades, research has increasingly focused on computational modeling to better understand fluid dynamics and transport mechanisms within lymphadematous tissues (Jayathungage Don et al. 2024). These models have ranged from zero to three-dimensional, each offering unique insights but often focusing on isolated aspects rather than the global behavior of the system. The first computational model of the lymphatic system was developed by Reddy (1977), where a one-dimensional framework based on the Navier–Stokes equations was used to model fluid flow in lymphatic vessels. Subsequent improvements were made by others. For instance, Macdonald et al. (2008) introduced a short chain of lymphangions to simulate a segment of the lymphatic pump. Bertram et al. (2020; Bertram and Davis 2023) further advanced this approach by incorporating a series of lymphangions separated by valves, where each valve's resistance was dynamically adjusted based on the pressure gradient across it. Notably, Contarino et al. (2018) incorporated the electrical activity of lymphatic vessel walls into a one-dimensional model of collecting lymphatics, coupling it with an electro-fluid-mechanical contraction (EFMC) model to simulate lymphatic contractions and valve dynamics across a range of pressure conditions.

As for higher-order models, Heppell et al. (2013, 2015) proposed a 2D model of the fluid flow through blood capillaries into the interstitium and its drainage by the lymphatic capillaries. Their model predicted a linear relationship between drainage flux and pressure difference between blood and lymphatic capillaries. Koudehi et al. (2023a) reconstructed a 3D model derived from micro-CT scans of the collecting lymphatics in the mouse hind limb. Their study aimed to investigate lymph propulsion and analyze fluid flow dynamics within the collecting vessel, as well as the deformation of the vessel wall and the poroelastic interstitium.

Due to the complexity of the lymphatic system and the limited available data on the biological mechanisms involved in lymphatic drainage, poroelastic models that analyze the global behavior of interstitial fluid in soft tissues are increasingly being explored (Kedarasetti et al. 2022; Sowinski et al. 2021; Greiner et al. 2021). By treating the tissue as a biphasic medium, consisting of a solid matrix and a fluid phase, poroelastic models have proven highly effective in modeling fluid drainage within soft tissues, particularly in lower limb lymphedema. Studies using such approach provided valuable insights into the effects of various compression techniques (Baish et al. 2022; Kaczmarek et al. 2015; Eymard et al. 2017; Koudehi et al. 2023b). For instance, Olszewski et al. (2011) developed a poroelastic model to study the effects of intermittent pneumatic pressure on the IFP and the fluid's velocity in an idealized geometry of the lower limb. Baish et al. (2022) incorporated the local vascular interactions between blood and lymphatic capillaries to model the IFP changes in the lower limb during lymphedema and compression therapy. These models were able to capture IFP changes inside the limb and provided insight on the effects of compression therapy. However, they have typically been limited to simplified, two-dimensional representations. This restricts their ability to accurately capture the 3D complexity of the lower limb.

This study aims at developing a 3D poroelastic model of the lower limb, designed to more accurately capture interstitial fluid dynamics and applied on a patient-specific geometry. Building on previous models that investigated the effects of compression therapy on patient-specific geometries in the solid phase only (Avril et al. 2010, 2012), the adopted poroelastic approach accounts for the fluid phase in soft tissues, which we believe is a critical factor in assessing compression efficacy. This model allowed for the analysis of fluid flow and tissue deformation under varying compression forces, providing deeper insight into the mechanisms that contribute to the effectiveness of compression therapy. The model was tested under baseline conditions, edema and lymphedema development, and therapeutic compression. By conducting a parametric study, we also analyzed the effects of different mechanical and hydromechanical properties of the soft tissues on lymphedema management.

In Sect. 2, we introduce the poroelastic formulation, the boundary conditions applied on the computational domain and the modeling approach for compression stockings. In Sect. 3, we present the model's predictions focusing on IFP, tissue permeability and volume change. Finally in Sect. 4 and 5, we discuss our results by comparing them to similar studies, address the model's limitations and draw our conclusions.

2 Methods

2.1 Problem formulation

Magnetic Resonance Imaging (MRI) scans were obtained from the University Hospital Center of Nice, France. They consisted of cross sectional images of a patient's lower limb, unaffected by lymphedema. The patient provided informed consent for the use of these images in this study.

The MRI scans were then segmented using 3D Slicer software, which allowed the identification of three layers of soft tissues: bones, muscle, and subcutaneous tissue (Fig. 1). Bone structures were excluded and instead represented by impermeable and fixed boundary conditions to replicate their rigid behavior.

The lymphatic system in the lower limb can be subdivided into two different systems: the superficial and the deep network (Pflug and Calnan 1971). The superficial network collects the fluid from the skin and the subcutaneous tissue while the deep network drains the subfascial area such as the muscles and the bones at a slower rate. In our model, we only focus on the superficial network where most of the fluid drainage in the lower limb occurs (Dayan et al. 2020). To incorporate this, we modeled the subcutaneous tissue as a poroelastic continuum, composed of a solid matrix phase coupled with a fluid phase. Muscle tissues were assumed impermeable and modeled as linear elastic. This assumption allows the simulation of fluid accumulation and drainage within the subcutaneous tissue only. In the following subsection, we present the governing equations of the poroelastic formulation.

2.1.1 Model of lymph flow

The fluid phase in the subcutaneous tissue was modeled using Darcy's law. The fluid velocity $\mathbf{u}$ is assumed to be driven by gradients of IFP and by gravity:

$$\mathbf{u} = -\frac{\kappa}{\mu}(\nabla p + \rho \mathbf{g}), \tag{1}$$

where κ is the hydraulic permeability of the tissue, μ is the fluid viscosity, $\mathbf{g}$ is the acceleration of gravity and p is the interstitial fluid pressure (IFP), representing the pressure

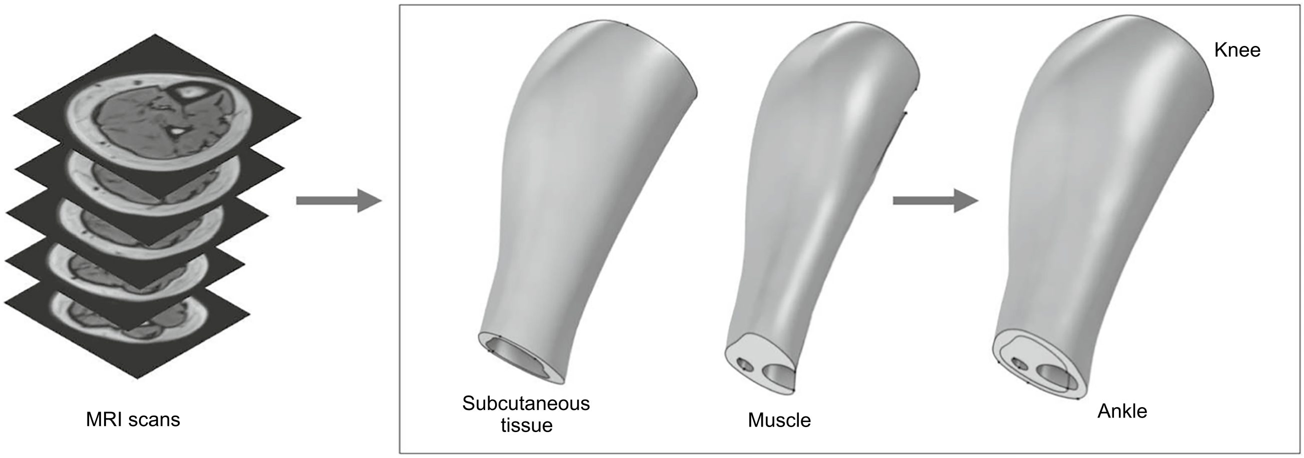

Fig. 1 Geometry reconstruction from MRI scans of a lower limb unaffected by lymphedema. The two bones, tibia and fibula, were excluded from the geometry and their boundaries were treated as rigid

within the fluid phase exclusively, distinct from the pressure in the solid phase.

In order to model pathological conditions, such as increased blood capillary pressures or lymphatic vessels obstruction, we included the vascular interactions between blood and lymphatic capillaries through the interstitial area. This was implemented using Starling's equation which states that a balance between oncotic and hydrostatic pressure in vessels determine the drainage and the production rate of the interstitial fluid (Taylor 1981). For simplification, we assumed that hydrostatic pressure is the main driving force for IFP dynamics. Therefore, we neglected the effects of oncotic pressure and considered that the interstitial fluid is a single fluid that can be filtrated from blood capillaries and drained into the lymphatic ones. Thus, in the subcutaneous tissue, blood and lymphatic capillaries were modeled as uniformly distributed sources (J_c) and sinks (J_L):

$$J_c = \beta_c(p_c - p), \tag{2}$$

$$J_L = \beta_L(p_L - p), \tag{3}$$

where β_c and β_L denote the wall permeability of blood and lymphatic capillaries, respectively, while p_c and p_L represent their internal pressures. Typically, $p_c > 0$ and $p_L < 0$ are assigned to modulate the effects of sources and sinks. Thus, the equilibrium between the values of these four parameters (p_c, p_L, β_c and β_L) will predict the rate of filtration or drainage of the interstitial fluid in the tissue.

Finally, the mass conservation equation is written as follows:

$$\nabla \cdot \mathbf{u} + \frac{\partial \phi}{\partial t} = J_c + J_L, \tag{4}$$

where $\mathbf{u}$ is Darcy's velocity and ϕ is the tissue porosity representing the fluid to solid ratio in the tissue. Table 1 summarizes the values of the hydromechanical parameters used in the simulations. Parameter values were taken from literature and ensured baseline conditions in our model. In this study, we assumed that the porosity is constant, hence the term $\frac{\partial \phi}{\partial t}$ is set to zero.

2.1.2 Elasticity equations

Assuming small strain and linear elasticity, the stress ($\boldsymbol{\sigma}_s$) strain ($\boldsymbol{\epsilon}$) relationship for a homogeneous and isotropic material is written as follows:

$$\nabla \cdot \boldsymbol{\sigma}_s = 2G\boldsymbol{\epsilon} + (K - \frac{2G}{3})\mathrm{tr}(\boldsymbol{\epsilon})\mathbf{I}, \tag{5}$$

where G is the shear modulus and K is the bulk modulus that are related to the Young modulus E and the Poisson's ratio ν by:

$$G = \frac{E}{2(1+\nu)}, \tag{6}$$

$$K = \frac{E}{3(1-2\nu)}. \tag{7}$$

Fluid pressure influences the volume change in the porous media. Conversely, the change in volume of the medium affects fluid pressure and velocity. Accordingly, the total stress in the porous tissue is the sum of the solid phase stress tensor $\boldsymbol{\sigma}_s$ and the fluid phase stress tensor $\boldsymbol{\sigma}_f = -p\mathbf{I}$. The force balance is then written as follows:

$$\nabla \cdot \boldsymbol{\sigma}_{tot} + \rho\mathbf{g} = \nabla \cdot (\boldsymbol{\sigma}_s - \alpha p\mathbf{I}) + \rho\mathbf{g} = 0, \tag{8}$$

where α is the Biot–Willis coefficient, representing how much of the applied pressure is transferred to the fluid phase inside a porous material.

The mechanical properties of each tissue were derived from literature (Frauziols et al. 2015; Rohan et al. 2013) and are summarized in Table 2.

Table 1 Baseline parameter values

Parameter	Description	Value	References
ρ	Density [Kg/m^3]	1000	–
μ	Viscosity [Pa.s]	0.001	–
ϕ	Porosity [-]	0.05	–
κ_0	Tissue permeability at zero strain [m^2]	10^{-14}	Baish et al. (2022)
M	Tissue permeability–strain coefficient [-]	12	Lai and Mow (1980)
β_c	Blood capillary conductance [1/Pa.s]	1.9×10^{-8}	Baxter and Jain (1989)
β_L	Lymphatic conductance [1/Pa.s]	9.47×10^{-8}	Baxter and Jain (1989)
p_{c0}	Reference blood pressure [mmHg]	10	Baxter and Jain (1989)
p_{L0}	Reference lymphatic pressure [mmHg]	– 2	Baxter and Jain (1989)
α	Biot–Willis coefficient [-]	1	–

Table 2 Mechanical properties of the soft tissues

	Skin	Fascia	Muscle	Sub. Tissue
Young Modulus (E)	0.60 MPa	0.599 MPa	0.012 MPa	0.009 MPa
Poisson's ratio (v)	0.49	0.49	0.47	0.48

2.1.3 Model of permeability

Previous modeling approaches often assumed a constant permeability in the tissue (Olszewski et al. 2011). However, as stated by Lai and Mow (1980), soft tissues exhibit a permeability that depends on the strain field induced by pressure gradients during flow. The permeability of the tissue changes according to pore dilation or compression. For example, when the tissue dilates due to high IFP, the pore spaces in the tissue increase leading to increased tissue permeability. We incorporated this behavior by using the following permeability–strain relation (Lai and Mow 1980):

$$\kappa = \kappa_0 \exp(Me), \tag{9}$$

where κ_0 is the tissue permeability at zero strain, $e \approx \frac{\Delta V}{V_0}$ is the dilatory strain, assuming isotropic deformation, and M is a parameter that determines the strength of the strain effect on κ.

Generally, tissue porosity can change as fluid enters or leaves the system. However, in our model we assume that the tissue maintains a constant porosity. Consequently, fluid accumulation or drainage is manifested in changes of IFP, volume and permeability values.

2.1.4 Model of compression stockings

In our model, we consider a compression stocking that exhibits uniform tension along the length of the limb. The stocking is represented by applying a pressure boundary condition on the skin, which would be referred to as the interface pressure.

Since we are dealing with patient-specific geometries, it is essential to account for the geometrical irregularities of the leg. In practice, when a compression garment is applied, the pressure experienced along the leg is not uniform. This variation arises due to the leg's conical shape, where the curvature radius increases from the ankle toward the knee. To capture this effect, the Laplace law is often used to estimate interface pressure in compression therapy by relating the pressure to the local radius of curvature and the tension in the fabric (Chassagne et al. 2019). Hence, the interface pressure (IP) applied in our model is derived from the Laplace law described below:

$$IP = \frac{T}{R_c}, \tag{10}$$

where T is the garment's tension and R_c is the curvature radius which varies depending on the leg's morphology (Avril et al. 2010; Gaied et al. 2006). While Laplace's law is useful for estimating pressure on realistic geometries, it relies on simplifying assumptions such as convex surfaces and no friction with the skin. Therefore, while it provides a first approximation, more advanced numerical models are needed for accurate patient-specific predictions (Chassagne et al. 2016).

2.1.5 Boundary conditions and numerical implementation

The computational domain simulating the lower limb is denoted by Ω, and Γ denotes its external boundary. γ_{ankle} and γ_{knee} denote the proximal boundaries at the ankle and the knee, respectively. At proximal boundaries (γ_{ankle} and γ_{knee}) we assumed that all soft tissues are constrained in the longitudinal direction and free to move horizontally. As for the subcutaneous tissue, the assumption of zero pressure was applied on γ_{knee}, representing an outflow of the interstitial fluid, meaning that the fluid can leave or enter the domain freely through this boundary (Fig. 2). All other boundaries were modeled as impermeable. These boundary conditions were chosen in order to prevent distal inflow and focus on the effect of proximal outflow during drainage.

The following equations summarize the pressure boundary conditions applied on the computational domain:

$$\frac{\partial p}{\partial n_\Gamma} = 0 \quad \text{in} \quad \Gamma, \tag{11}$$

$$\frac{\partial p}{\partial n_\gamma} = 0 \quad \text{in} \quad \gamma_{ankle}, \tag{12}$$

$$p_{knee} = 0, \quad \text{in} \quad \gamma_{knee}. \tag{13}$$

Finally, the constructed geometry was imported into COMSOL Multiphysics® v.6.0 in which the mesh was generated and the different tissues along with their mechanical properties were defined. The Porous Media Flow module was used to model poroelasticity. Quasi-static and temporal studies were conducted using linear elastic solid mechanics coupled with a fully transient Darcy's law. Sources and sinks depicting lymphatic and blood capillaries were modeled by adding mass sources to Darcy's model. The skin and the fascia were modeled as elastic membranes. The compression stocking was modeled as an external pressure applied on the skin and gravity was applied on all fluid and solid volumes. We performed a mesh sensitivity analysis to ensure the accuracy and stability

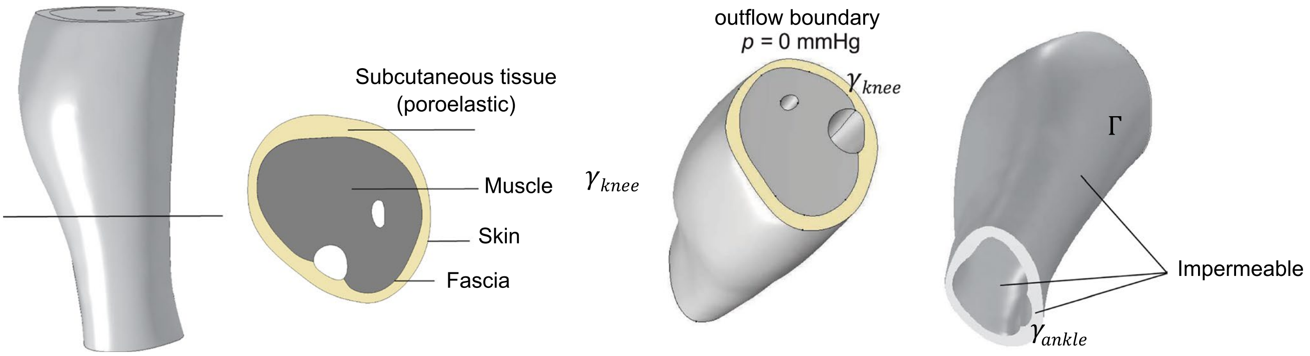

Fig. 2 Illustration of the boundary conditions applied on the computational domain

of the numerical simulations. Seven mesh densities were tested with 6 459, 12 627, 25 796, 62 643, 175 288, 399 524, and 1 022 857 tetrahedral elements. Mesh convergence was evaluated by calculating the L^2 norm of the IFP error across successive mesh refinements, with a tolerance set to 0.001. The mesh containing 175,288 tetrahedral elements and 22,220 triangular elements was ultimately selected as it satisfied the accuracy requirement while maintaining computational efficiency.

3 Results

3.1 Simulation of baseline conditions

We first simulated a baseline condition where we considered that the fluid filtered by blood capillaries is fully drained by the lymphatic capillaries. Using Eqs. 2 and 3, the baseline conditions can be represented by:

$$J_c + J_L = 0. \tag{14}$$

Using Eq. 14, the IFP can then be calculated using:

$$p = (\beta_c p_c + \beta_L p_L)/(\beta_c + \beta_L). \tag{15}$$

This formulation serves as a simplified baseline estimation of the IFP in equilibrium. For baseline conditions, we set $p_c = p_{c0} = 10$ mmHg and $p_L = p_{L0} = -2$ mmHg. All other parameters were assigned their baseline values as listed in Table 1. In order to assess the effects of gravity on the IFP distribution, the baseline condition was tested with and without the presence of gravitational forces. Figure 3 shows the IFP distribution in the 3D computational domain of the subcutaneous tissue as well as the longitudinal distribution against the normalized length of the anterior side of the limb.

In the absence of gravity, the results show that the baseline IFP remained around 0 mmHg as predicted by Eq. 15. When gravitational forces were added, a higher IFP value was observed at the ankle level, highlighting the presence of gravity-driven fluid pooling. Figure 4 illustrates the Darcy's velocity magnitude of the fluid in both cases, with and without gravity, highlighting the effects of gravity in redirecting and increasing the velocity of the flow toward the ankle, which lead to an increase in the IFP, from 0 mmHg (in the absence of gravity) to 0.65 mmHg and around 1% change in cross section area around the ankle region.

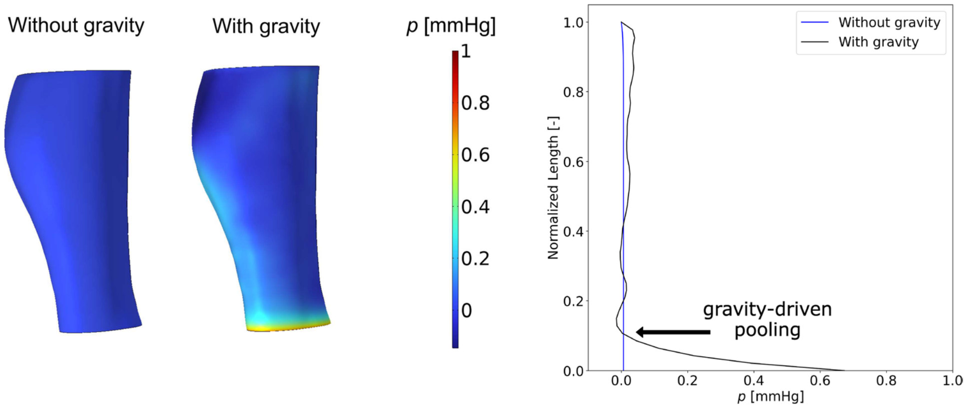

Fig. 3 Quasi-static simulations of the baseline conditions ($p_c = 10$ mmHg and $p_L = -2$ mmHg) with and without the effects of gravity. The graph shows the IFP distribution plotted against the normalized length of the leg's longitudinal anterior side, where 0 represents the ankle level and 1 the knee level

3.2 Simulation of edema and lymphedema conditions

To simulate edema conditions, we considered the case where the fluid filtered by the blood capillaries is not adequately drained by the lymphatic ones. Accordingly, we maintained gravity and we increased the blood capillary pressure p_c while maintaining a basal lymphatic pressure $p_L = p_{L0}$.

Figure 5 illustrates the pressure distribution along the length of the leg for different values of p_c. The results show that IFP increases with the increase in p_c, in accordance with Eq. 15 (IFP = 5.1 mmHg for $p_c = 40$ mmHg and IFP = 11.8 mmHg for $p_c = 80$ mmHg). In addition, higher fluid pressure was observed around the ankle level due to gravity. In Fig. 6, we compared the cases of $p_c = 40$ and $p_c = 80$ mmHg, with and without gravity. The results highlight differences in IFP

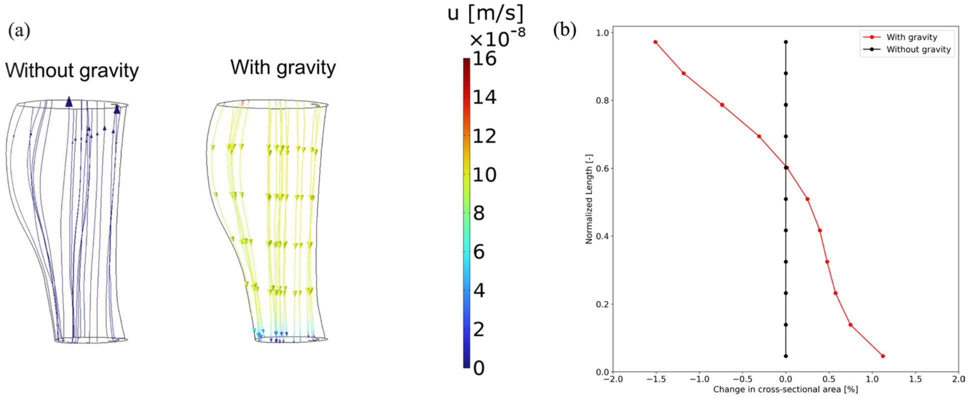

Fig. 4 **a** Visualization of Darcy's velocity plot lines showing the effects of gravity on the fluid velocity direction and magnitude in baseline conditions. **b** Change in cross section area along the length of the leg in basal conditions with and without the presence of gravity

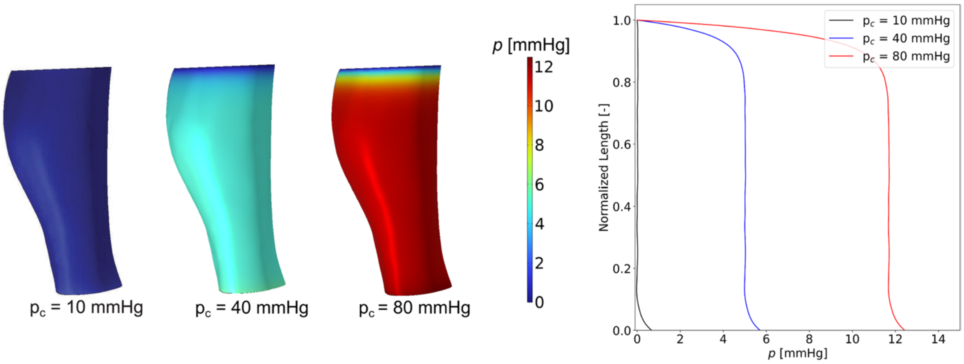

Fig. 5 Quasi-static simulations of edema conditions, represented by an increase in blood capillary pressure (p_c). Two values of p_c were simulated, 40 mmHg and 80 mmHg and were plotted against the baseline p_c value (10 mmHg)

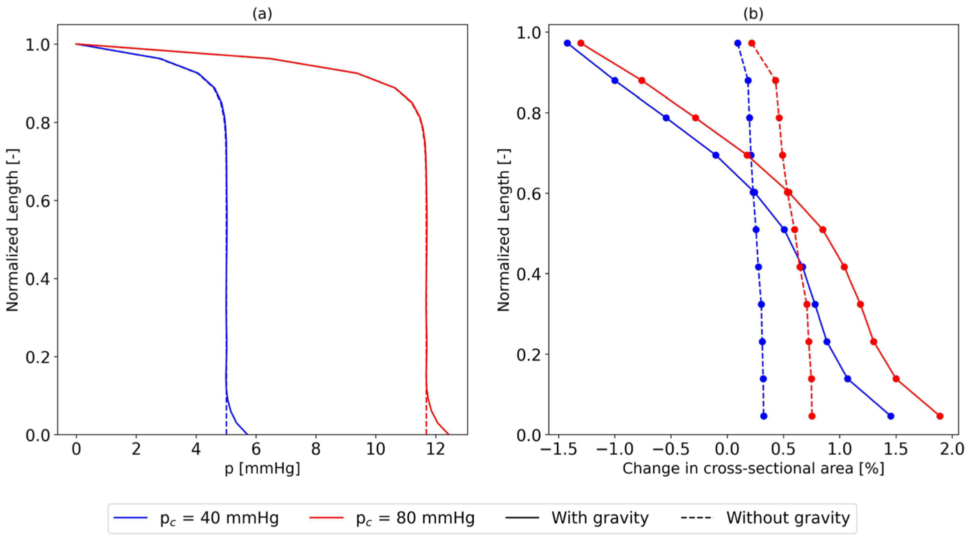

Fig. 6 **a** Interstitial fluid pressure (IFP) distribution and **b** relative change in cross sectional area along the normalized length of the leg for two values of p_c with and without gravity during edema

distribution, with a notable increase in cross sectional area observed when gravity is included, indicating greater fluid accumulation in the lower limb.

Figure 7 shows the effects of varying p_{knee} on IFP. Notably, while the IFP distribution remained uniform along the leg, the IFP value on the knee level was influenced by the value of p_{knee}.

Comparatively, we simulated lymphedema by modeling a blockage of lymphatic pathways, a condition which can arise when one or several lymph nodes are removed during lymphadenectomy. In this case, the lymphatic capillaries represented by the sink term in Eq. 4 were removed from the model. Figure 8 shows the IFP distribution and corresponding changes in cross sectional area for p_c values of 40–80 mmHg, in the absence of lymphatic drainage. As expected, a higher p_c value result in increased interstitial fluid pressure and more pronounced expansion of the cross sectional area.

Since experimental data on subcutaneous tissue permeability were unavailable in this study, we analyzed its impact on fluid accumulation across a range of values reported in literature for subcutaneous tissue modeling (Olszewski et al. 2011; Eymard et al. 2017). Figure 8 shows the effects of tissue permeability at zero strain (κ_0) on IFP with and without gravity.

Figure 9 shows that, in the absence of gravity, higher permeability values lead to a less pronounced increase in IFP during edema compared to lower permeability values, where the IFP was in agreement with the value predicted by Eq. 15. For example, at the ankle level, for $\kappa_0 = 10^{-11}$ m^2 the IFP was around 1 mmHg while for $\kappa_0 = 10^{-15}$ m^2, the IFP was equal to 5 mmHg. This suggests that for higher tissue permeability, fluid can drain more easily through the tissue toward the outflow boundary at the knee level. On the other hand, in the presence of gravity, higher permeability values were associated with more significant gravity-driven fluid pooling at the ankle. This is due to more significant dilation of the interstitial pore space at higher permeability values. With higher permeability values, the effects of gravity dominated the effects of the local absorption and filtration driven by the vascular interactions. Subsequently, we observed that vascular interaction dominates when the tissue permeability is low.

Fig. 7 **a** Interstitial fluid pressure (IFP) distribution and **b** relative change in cross sectional area along the normalized length of the leg for three values of p_{knee}

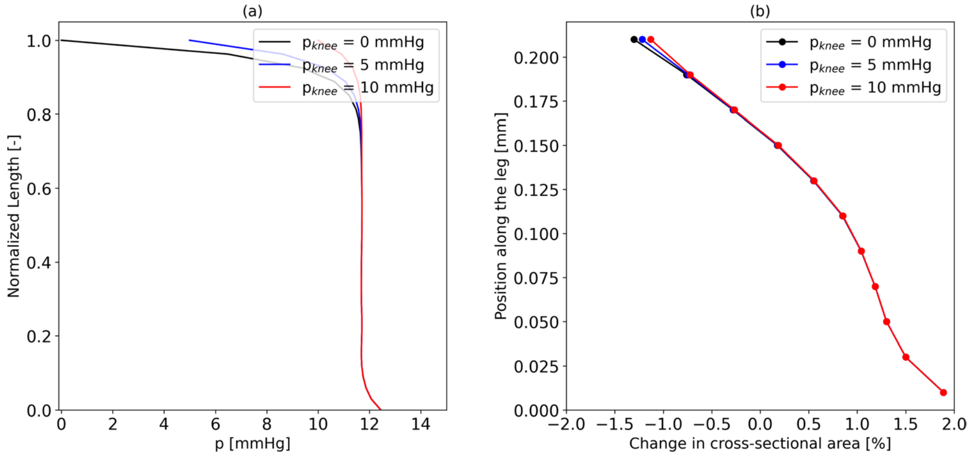

Fig. 8 **a** Interstitial fluid pressure (IFP) distribution and **b** relative change in cross sectional area along the normalized length of the leg for two values of p_c in the case of lymphedema

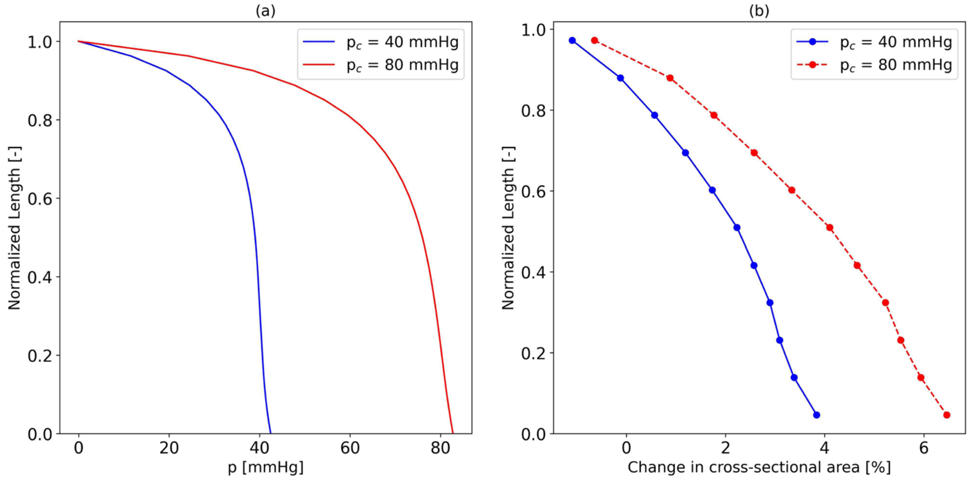

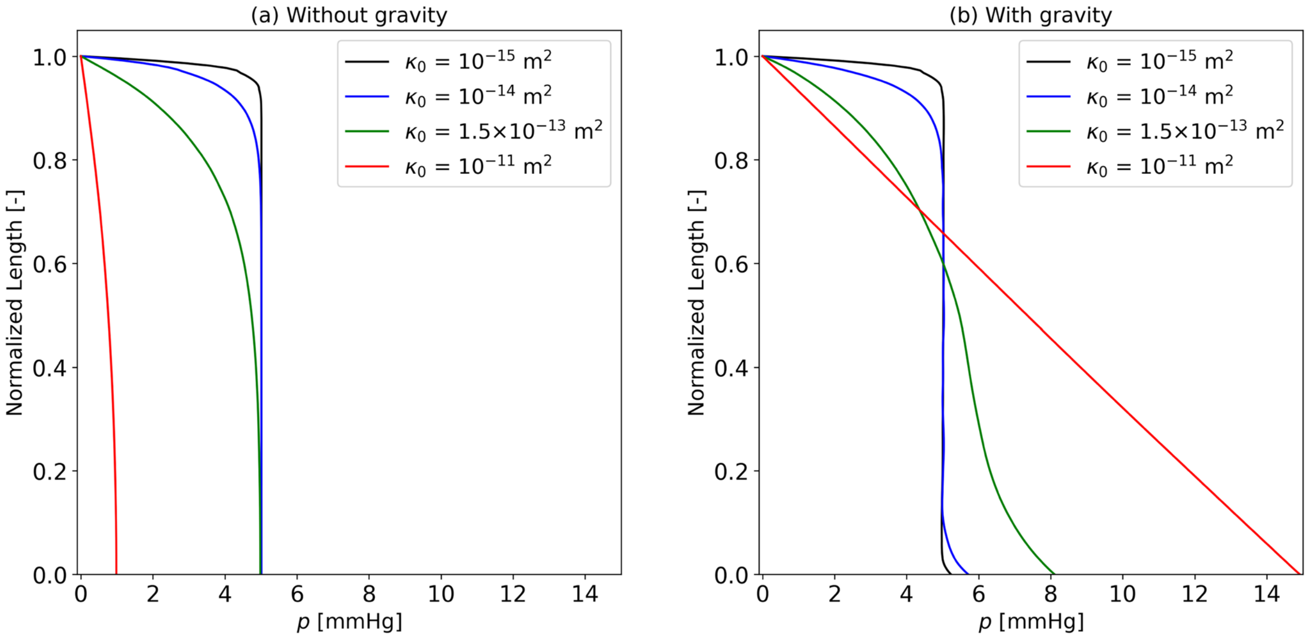

Fig. 9 Parametric study on the effects of tissue permeability (κ_0) on IFP during edema conditions, **a** without and **b** with gravity

Fig. 10 Bar plots showing the percentage of volume increase (**a**) and the values of tissue permeability (**b**) for each value of p_c simulated in lymphedema condition. The bars in red show the case where the lymphatic sinks were omitted and only the blood capillaries sources were modeled

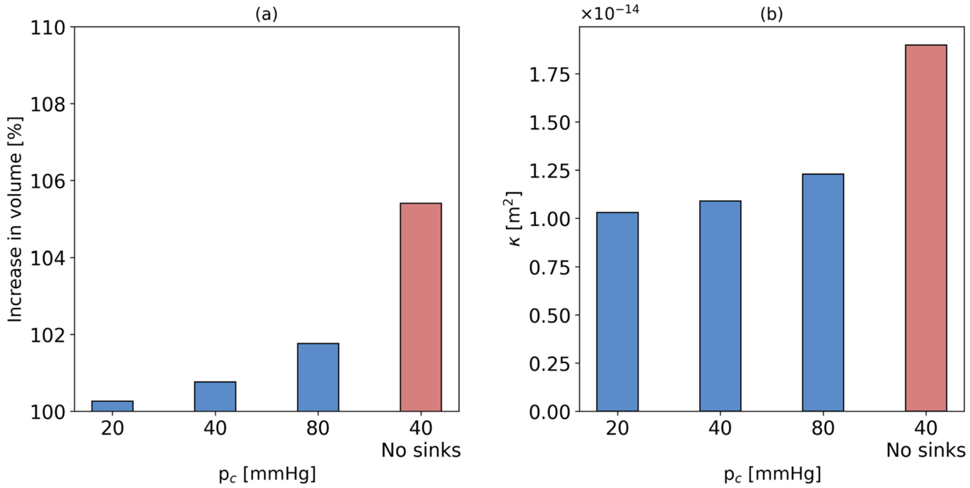

Figure 10 illustrates the increase in volume and average tissue permeability for different p_c values used to model edema formation. The results show that the lymphedema condition, where the sinks were removed from the model, lead to more significant volume increase (5.8 %) compared to the conditions where sinks were still present (< 2%). For the same value of $p_c = 40$ mmHg, the IFP in the leg was equal to 40 mmHg in the absence of the lymphatic capillaries compared to 8 mmHg in the case where the lymphatic capillaries were present. This underscores the key role of the local lymphatic capillaries in fluid drainage and preventing volume increase in the limb.

3.3 Compression application

3.3.1 Effects of whole-limb compression on IFP

To accommodate different clinical needs, compression stockings are classified into different categories based on the level of pressure they provide. Lower pressure classes are typically recommended for mild cases, while higher pressure classes are required for more advanced stages. Herein, we studied three different values of pressure corresponding to mild ($p_w = 10$ mmHg), moderate ($p_w = 30$ mmHg) and strong compression ($p_w = 50$ mmHg) (Partsch

2012). Firstly, we applied a uniform compression on the whole computational domain of the lower limb. The initial configuration corresponded to a simulated edematous leg with $p_c = 40$ mmHg. Figure 11 shows the IFP distribution along the length of the leg for different p_w values.

We observed that the effect of compression on IFP distribution were more pronounced with the increase in p_w. With higher p_w values, the compression tended to uniformly distribute the IFP along the leg, by increasing the pressure around the knee level and decreasing it at the ankle level. Nevertheless, the effects of compression were not very significant on the interstitial fluid drainage since we are depicting the case of a tissue permeability value where vascular interaction dominated over the gravity effects ($\kappa_0 = 10^{-14}$ m^2). Moreover, by simulating a continuous increased blood capillary pressure ($p_c = 40$ mmHg) even after compression application, the results suggest that compression application alone did not drain the excess of fluid in the tissue through the open outflow boundary.

Next, we investigated the effects of varying Poisson's ratio on the model outcomes. The values were selected based on those used in previous poroelastic models of lymphedema (Baish et al. 2022; Olszewski et al. 2011). Figure 12a shows the effects of Poisson's ratio of the subcutaneous tissue on the IFP distribution after compression application. Interestingly, when applying the same compression to a more compressible tissue (represented by a smaller Poisson's ratio) the effects were significantly more pronounced. Figure 12b shows the same comparison between two Poisson's ratio values but for a higher tissue permeability at zero strain value ($\kappa_0 = 1.5 \times 10^{-13}$ m^2). In this case, results show that compression was much more effective in restoring the dominance of local vascular interactions and counteracting the effects of gravity. For example, for $\nu = 0.33$, the IFP around the ankle was reduced from 8 mmHg to 5.2 mmHg after compression application. Figure 13 demonstrates that this was achieved by reducing leg volume, which in turn decreases tissue permeability. By compressing the leg tissues, the pore spaces are reduced, leading to a decrease in

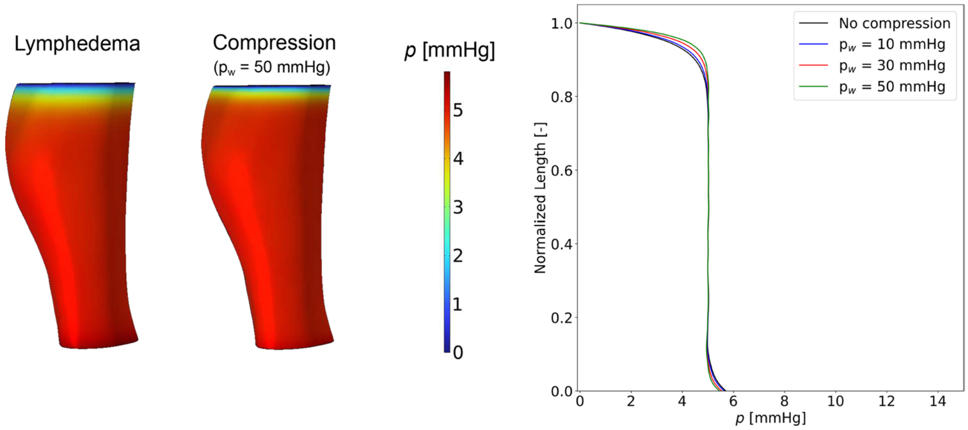

Fig. 11 Quasi-static simulations of compression application compared with a edema condition ($p_c = 40$ mmHg). The graph shows the IFP distribution for different external pressure values (p_w) corresponding to different classes of stockings. The edema condition was simulated by increasing the blood capillary pressure ($p_c = 40$ mmHg). The compression was then simulated with edema condition as an initial state

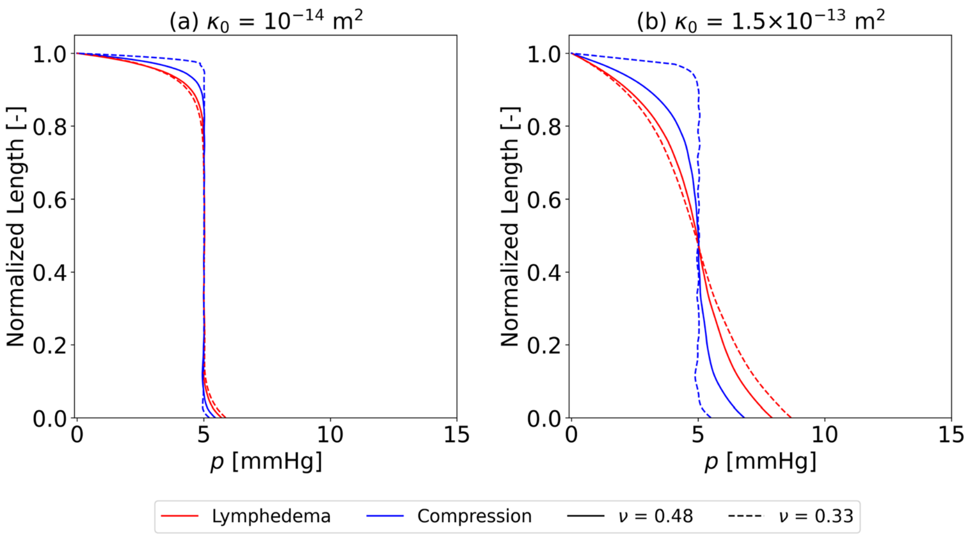

Fig. 12 Parametric study of the effects of Poisson's ratio of the subcutaneous tissue on the IFP. For each value of permeability, two values of Poisson's ratio were studied to simulate edema conditions and compression application

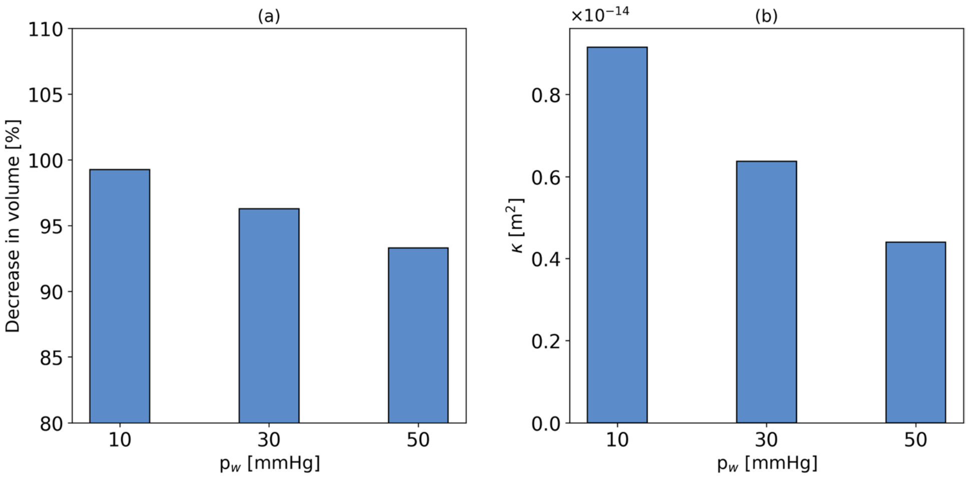

Fig. 13 Bar plots showing the percentage of volume decrease (**a**) and the values of tissue permeability (**b**) for each value of external pressure (p_w) simulated

permeability. The results suggest that higher compression pressure effectively mimics the effect of lower permeability, reinforcing local vascular interactions and preventing fluid accumulation at the ankle level.

3.3.2 Geometrical heterogeneity

In this section, compression was simulated by applying an interface pressure on the skin, derived from Laplace's law (Eq. 10), which accounts for the geometric shape and curvature of the leg. According to this principle, regions with a smaller radius of curvature experience higher compression pressures. In this example, we took the stocking's tension to be uniform along the leg ($T = 0.4$ N/mm). Conversely, the pressure exerted by the compression device is not uniform along the leg but instead varies based on the leg's morphology.

Starting from the initial configuration of a lymphadematous leg with $p_c = 40$ mmHg, we applied the Laplace derived pressure in our model. Figure 14 shows the resulting IFP distribution of the Laplace compression compared to the application of a uniform compression on the whole domain. We observed that free-standing fluid at the ankle level was significantly reduced under Laplace compression even though the distribution was not uniform. Consequently, we could conclude that vascular interaction is restored at the ankle level under Laplace compression while the area closer to the knee level was not much affected and the IFP remained around their initial values. This is due to the fact that the radius of curvature is bigger at the knee level which means that the pressure applied by the compression stocking is less than on the ankle level.

3.3.3 Temporal evolution of IFP during edema and whole-limb compression

In this section, we analyzed the temporal evolution of edema formation, as well as the effects of whole-limb compression therapy on interstitial fluid drainage. First we simulated the development of edema during time with the presence of gravity. Figure 15a shows the evolution of IFP at two points of interest in the limb, under the knee level (A) and at the ankle level (B). The initial state of the model (t = 0 s) corresponded to the baseline conditions of $p_c = 10$ mmHg and $p_L = -2$ mmHg under gravity effects. To simulate edema p_c was set at 40 mmHg, $p_L = -2$

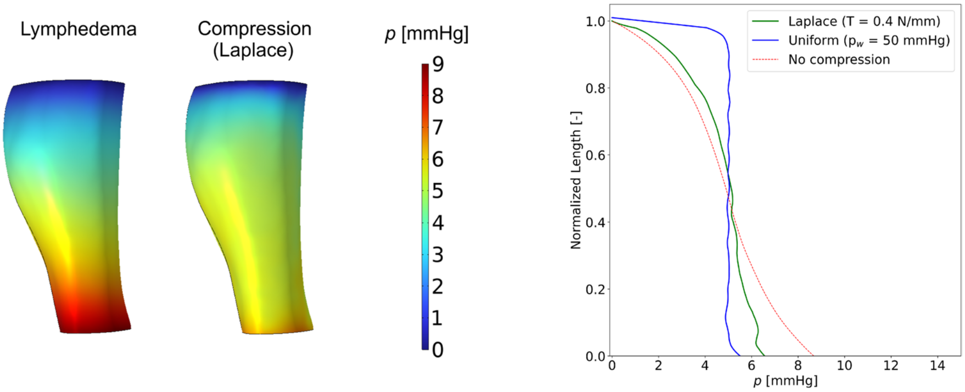

Fig. 14 Comparison between IFP distribution after a uniform and a Laplace derived compression application in the presence of gravity. The edema condition was simulated by increasing the blood capillary pressure (p_c = 40 mmHg). The compression was then simulated by taking the numerical simulated edema as an initial state

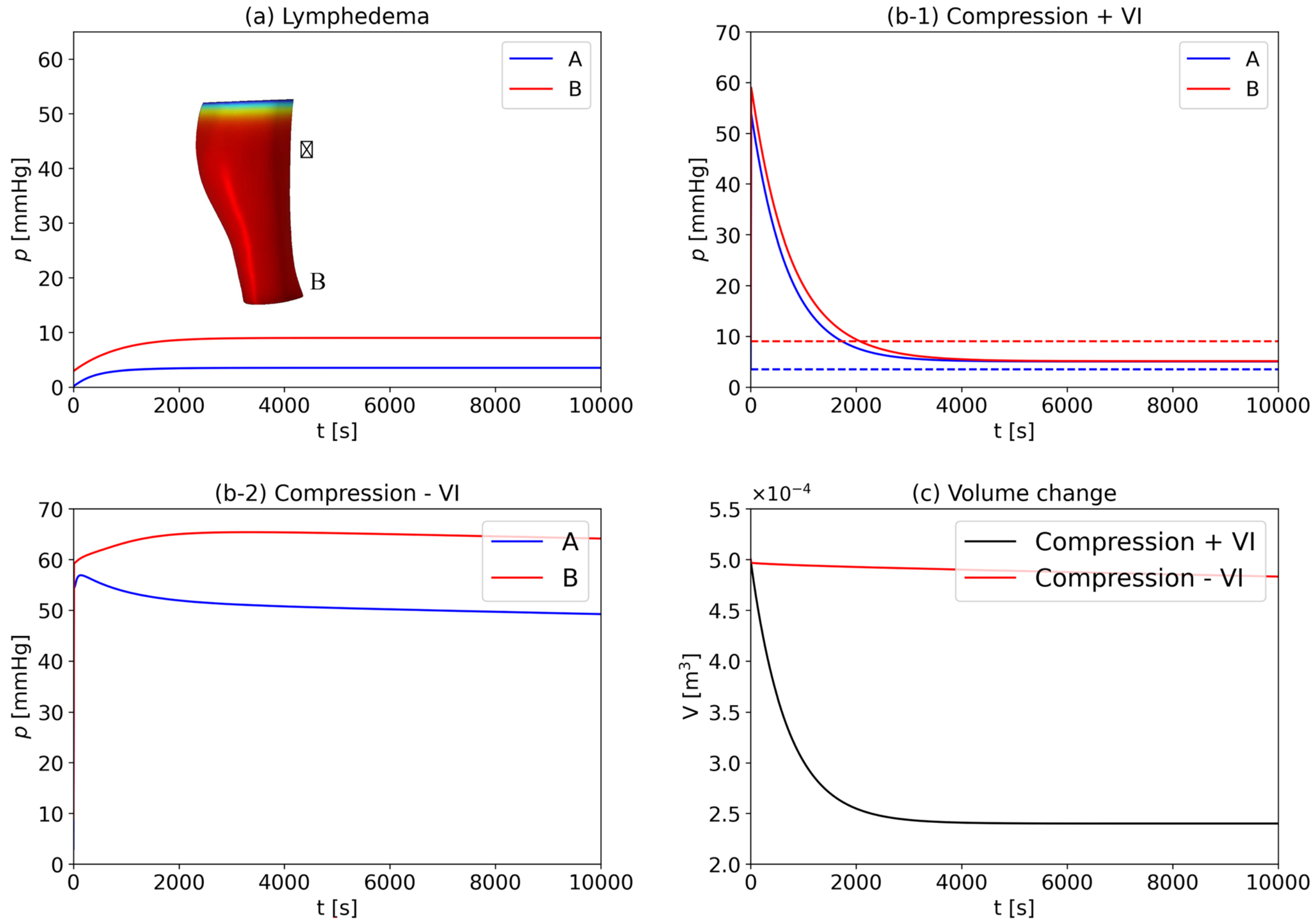

Fig. 15 Temporal evolution of IFP at two control points A and B, during **a** edema conditions, **b-1** after compression application (p_w = 50 mmHg) , in the presence of gravity and local vascular interactions (VI), **b-2** after compression application and by omitting the local lymphatic sinks from the model. The graph **c** shows the temporal evolution of the limb's volume during simulations of cases (b-1) and (b-2)

mmHg, $\kappa_0 = 1.5 \times 10^{-13}$ m^2 and $\nu = 0.33$. At both points, IFP increased during time until it reached an equilibrium depending on the point's location in leg. Then, we simulated the application of compression while including local vasculature (J_c and J_L), allowing fluid drainage through the open boundary and via local lymphatic sinks simultaneously (Fig. 15b-1). Compression was applied gradually by increasing linearly to reach p_w value after 10 s of the simulation and was then kept constant. Initially, IFP increased at both points (up to 60 mmHg) as compression was applied along the entire leg. Over time, IFP gradually decreased until reaching equilibrium at approximately 5 mmHg, indicating the restoration of local vascular interactions. Finally, we removed the local lymphatic sinks to model a total blockage of lymphatic pathways, meaning fluid could only drain through the open boundary at the knee level (Fig. 15b-2). In this case, IFP increased initially during time but took significantly longer time to decrease and stabilize than the case of Fig. 15b-1. This highlights the critical role of local vessels in restoring IFP values in the lower limb during lymphedema management. Figure 15d depicts the evolution of limb volume in both cases. When local drainage was present, the leg volume decreased more rapidly due to both local and open boundary drainage, aided by compression. In the absence of local drainage, volume reduction occurred more slowly, emphasizing the limited effectiveness of compression when lymphatic function is impaired.

3.3.4 Temporal evolution of IFP during partial compression

Finally, we tested the application of external compression on only part of the limb to examine how fluid moves from the compressed to the uncompressed region. In this case, vascular interaction was not modeled in order to emphasize the sole effect of compression on fluid drainage, meaning that fluid drainage was only possible through

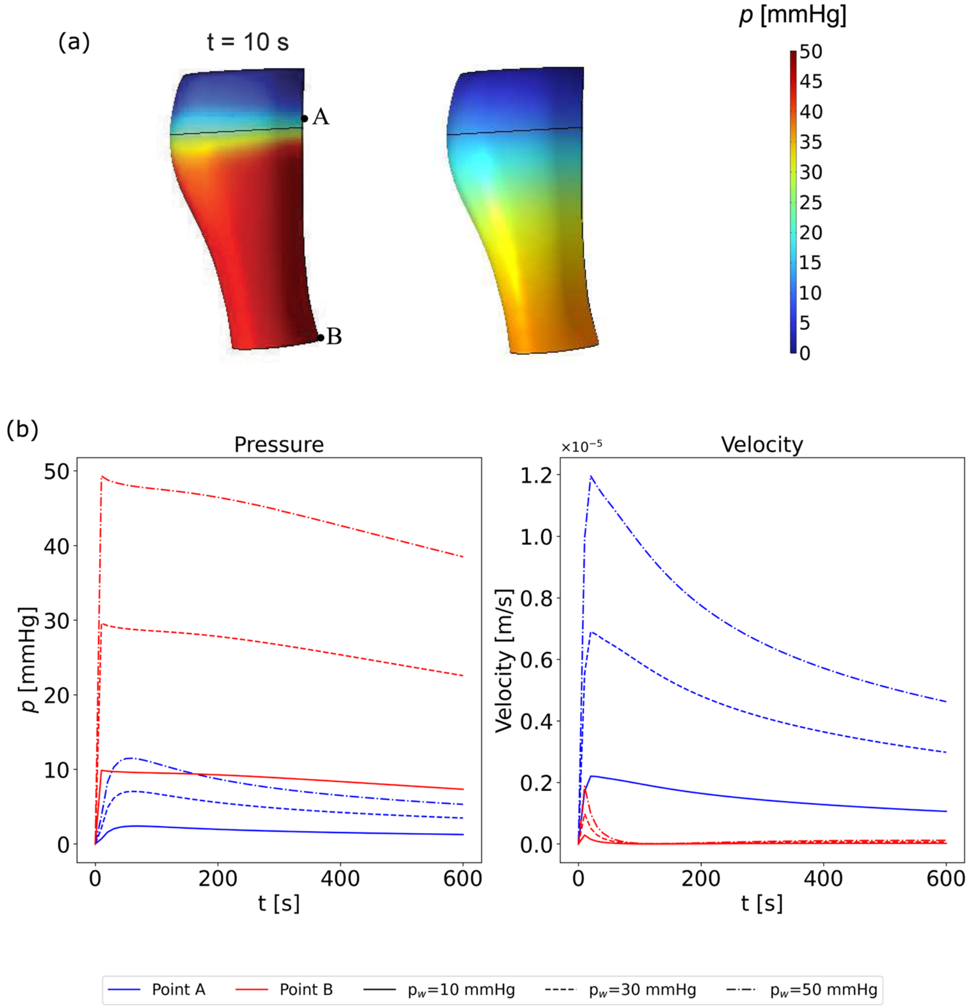

Fig. 16 **a** Time-dependent simulations of compression application at two time instants (t = 10 s and t = 600 s). Compression was applied on part of the leg (from point B until right below point A). **b** Temporal evolution of IFP and Darcy's velocity at two control points A and B for three different values of p_w

the open outflow boundary. The compression was applied to the region extending from the ankle to below the knee level (Fig. 16a). We analyzed velocity and pressure at two points of interest: the ankle level (point B) and the area just above the compression stocking (point A). Figure 16b presents the pressure and velocity values for different levels of compression. As expected, higher compression pressures resulted in greater increases in IFP and velocity. The results indicate that after applying compression, pressure in the compressed region initially rose to a higher IFP value (50 mmHg at point B - under compression - and 12 mmHg at point A - above compression -) before gradually decreasing over time. Velocity, on the other hand, initially increased before dropping to zero. In the region above the compression, pressure also increased, though to a lesser extent, while velocity showed a more pronounced rise before declining. This suggests that fluid is pushed from the compressed region into the uncompressed area, highlighting its drainage through the open boundary.

4 Discussion

This study demonstrates the potential of a poroelastic approach to deepen our understanding of the development and management of lower limb lymphedema. First, by simulating edema conditions, we illustrated the accumulation of interstitial fluid and the increase in interstitial fluid pressure (IFP) within the subcutaneous tissue. The results indicated that IFP increases with the increase in blood capillary pressure, leading to fluid build-up and a corresponding increase in leg volume (Guyton et al. 1971; Guyton 1965). Additionally, we modeled a complete blockage of local draining lymphatics to simulate lymphedema conditions, and observed significantly higher IFP values accompanied by a more pronounced increase in leg volume, highlighting the crucial role of local drainage in stabilizing IFP and limiting volume expansion during lymphedema progression. The pressure and volume changes predicted by our model can be compared with experimental values reported in literature (Suehiro et al. 2013; Lu et al. 2014). In particular, Lu et al. (2014) documented the volume change in lower limb's soft tissues in patients with lower limb secondary lymphedema for different stages of the disease. They reported that in early stages, the difference of volume between the affected and the unaffected limb is around 1% and it increases up to 9% in the second stage. Our model predicted a volume change ranging from 0.3–2% when simulating an increase in blood capillary pressure. Furthermore, the model offers the possibility to simulate the development of lymphedema due to different factors. For example, increasing the lymphatic pressure to depict a loss in drainage capacity or an increase in blood capillary wall permeability which can arise due to inflammation could help studying different pathologies leading to secondary lymphedema.

By incorporating the effects of gravity, our results showed how gravitational forces influence IFP and fluid velocity between standing and supine positions. We also examined the impact of different tissue permeability values, revealing that higher permeability in the standing position exacerbates gravity-driven fluid pooling at the ankle, consistent with previous literature numerical findings (Baish et al. 2022). When permeability is high, gravity dominates over local vascular interactions, leading to fluid accumulation in the leg. Conversely, lower permeability prevents excessive fluid accumulation at the ankle, maintaining the dominance of local vascular interactions.

When simulating compression therapy, our model successfully reproduced the expected reduction in leg volume and the redistribution of IFP (Gianesini et al. 2020). The parametric study demonstrated that the redistribution of IFP depends on tissue permeability. With higher permeability, compression drains interstitial fluid more effectively and prevents gravity-driven pooling at the ankle. When applying compression derived from Laplace's law to account for the leg's morphology, we observed higher interface pressure at the ankle, which helped eliminate free-standing fluid and restored the dominance of vascular interactions over gravitational forces. This is due to the fact that the ankle has a smaller curvature radius than the knee, leading to a higher localized pressure, which in turns enhances fluid drainage. These findings could aid in optimizing external pressure gradients for effective fluid drainage. Since compression therapy requires a balance between patient comfort and therapeutic efficacy, we believe that incorporating individual leg morphology into simulations is crucial for developing personalized treatment strategies for lower limb lymphedema.

The strain-permeability relationship (Eq. 9) implemented in our model provided a representation of permeability changes during fluid accumulation and drainage. As observed by Lai et al.(Lai and Mow 1980), tissue permeability depends on fluid flow within the tissue. Indeed, permeability increases with fluid accumulation and volume expansion, and decreases under compression. This underscores a key function of compression stockings in lymphedema management which is the reduction in tissue permeability to counteract gravity-driven fluid pooling at the ankle. The parametric study on Poisson's ratio further indicates that compression is less effective in tissues with lower compressibility. This corroborates with clinical observations showing that in the early stages of lymphedema, when the tissue remains compliant, compression therapy is more effective (Mosti and Partsch 2013). However, as the disease progresses the tissue becomes stiffer and less compliant which would diminish the efficacy of compression as a treatment. Incorporating tissue remodeling into the model could improve predictions of compression therapy outcomes across different stages of lymphedema.

The temporal evolution of IFP during edema simulation indicates an initial increase followed by a plateau, as equilibrium is established between blood and lymphatic pressure and the IFP. Since the model assumes static tissue hydromechanical behavior, pressure stabilizes once equilibrium is reached, with pressure and volume remaining constant. The time to reach equilibrium in our model appears faster than that reported by Baish et al. (2022). We believe that this difference is primarily due to the higher permeability value used in our simulations, which leads to a faster equilibrium and fluid redistribution within the tissue.

Even though tissue remodeling during time is not considered, the study still offers valuable insights into the time course of pressure build-up in the leg following a disturbance. Numerical results showed that when compression is applied, IFP initially spikes before gradually decreasing to a new equilibrium. This new equilibrium is characterized by a uniform IFP in the lower limb, eliminating the gravity effects of fluid pooling at the ankle. In another simulation, we investigated a scenario in which local drainage mechanism was eliminated, allowing fluid drainage only through the subcutaneous tissue's open boundary. In this case, the pressure increase following compression application was significantly slower in reaching equilibrium. This highlights the critical role of local vascular interactions, modeled here as lymphatic sinks, in facilitating interstitial fluid drainage, as also noted by Baish et al. (2022). The numerical results obtained from applying compression to part of the leg, in the absence of vascular interactions, align with the findings reported in Olszewski et al. (2011). These simulations could help to assess the time required for an adequate fluid drainage during pneumatic compression (Phillips and Gordon 2019).

Although the model provided qualitative predictions consistent with the literature, it relies on assumptions and has limitations. Notably, the modeled vascular interaction between the blood and the lymphatic capillaries was based on Starling's equation, which is a simplification of the biological mechanisms involved in the drainage process. In addition, compression therapy has been shown to reduce or prevent venous reflux by improving venous valve competence. This restoration of unidirectional flow helps reduce venous pooling and prevents the resulting increase in capillary hydrostatic pressure, thereby mitigating excessive fluid filtration into the interstitial space (Partsch and Partsch 2005). Incorporating this phenomenon requires a complex and explicit modeling of the blood and lymphatic vessels but would eventually make the model more accurate and able to reproduce more realistic mechanisms. The model also assumes isotropic and uniform tissue permeability and porosity, even though experimental data suggest that porosity is likely higher in regions of fluid accumulation. Incorporating medical imaging data on initial fluid distribution could improve model accuracy, especially for drainage simulations where fluid would be expected to migrate from high permeability regions toward less fluid-saturated areas. Another simplification in our model is the assumption of zero pressure on the upper surface of the subcutaneous tissue. This assumption was adopted to emphasize local interactions between blood and lymphatic capillaries. Alternative pressure values were tested, demonstrating that while gravity effects remain consistent, IFP distribution varies according to the pressure value applied on the boundary. Future refinements could incorporate more accurate pressure data at the knee level.

The vascular interaction model was based on the assumption of a uniform distribution of fluid sources and sinks within the tissue. In reality, initial lymphatics primarily facilitate drainage, and capillaries are predominantly located in the superficial tissue beneath the skin, especially around the ankle (Schacht et al. 2009; Shinaoka et al. 2020). Incorporating more detailed data on blood and lymphatic capillary distribution in the lower limb could allow for a more realistic implementation. We hypothesize that a nonuniform IFP distribution would emerge, depending on the initial spatial arrangement of these sources and sinks. While our model assumes a constant subatmospheric suction pressure at the lymphatic outlet, experimental and computational studies have demonstrated that, in reality, collecting lymphatic vessels actively generate transient suction during contraction. This active pumping mechanism enables fluid uptake under low interstitial pressures and plays a critical role in lymphatic drainage, which should be considered in future model refinements. (Jamalian et al. 2017). While this was simplified by the use of a constant subatmospheric sink pressure in our model, future work could incorporate time-dependent boundary conditions to more accurately capture lymphatic pumping behavior. Additionally, the model does not account for the anisotropic properties of soft tissues in the leg. Implementing an anisotropic tissue mechanics law would likely alter the pressure distribution, as deformation under compression or fluid accumulation would be nonuniform.

The model offers the possibility for future improvements and refinements. For example, it is established that muscle contractions facilitate fluid drainage in the lower limbs by increasing tissue pressure and enhancing lymphatic drainage, hence, incorporating this mechanism could predict fluid drainage during physical activity. This could be achieved by imposing a time-dependent pressure on the internal boundaries of the muscle (Rohan et al. 2015). An important aspect of this modeling approach is the interplay between blood capillary fluid flux and lymphatic drainage, particularly under compression. Depending on the modeling conditions, external compression may act by reducing transcapillary filtration, increasing lymphatic drainage, or both. Future extensions of this work could include more refined descriptions of capillary and lymphatic regulation to better quantify their respective roles in fluid volume changes under compression. Moreover, while the skin is currently modeled as a membrane element, in reality, some lymphatic drainage occurs within the skin. This could be achieved by including the skin as a 3D biphasic layer, improving the accuracy of drainage simulations. Future extensions could also consider blood vessels which could allow simulations of vascular diseases that contribute to fluid accumulation, further advancing our understanding of the mechanisms underlying lymphedema formation. Finally, to further validate our model, a comparison of volume changes between healthy and lymphedematous limbs will be conducted, providing a quantitative assessment of fluid drainage, accumulation and redistribution under different conditions. Experimental data derived from bioelectrical impedance analysis, a valuable tool to assess volume change during time (Montalibet et al. 2020), would help us validate our model and tune it to give more accurate predictions. Although in this study we presented the results of only one anatomically realistic geometry, the long-term goal of this work is to develop a patient-specific computational framework that can be applied to multiple subjects, allowing for customized analysis of interstitial fluid dynamics. This would help us explore subject-specific response to compression treatment, i.e., how compression is influenced by the thickness of each soft tissue and their mechanical parameters.

5 Conclusion

This study explored the fluid and pressure dynamics associated with lower limb lymphedema and the effects of compression therapy. By simulating increased capillary pressure or lymphatic obstruction, the model highlighted mechanisms of fluid accumulation, pressure increases, and volume changes in the leg, providing insights into common clinical presentations of lymphedema. Findings suggest that while compression therapy impacts IFP, it may be insufficient alone for complete fluid drainage, especially without local vascular contributions. This underscores the importance of considering the combined role of vascular and lymphatic interactions in treatment strategies. Limitations of the model, such as the assumption of uniform permeability and isotropic tissue properties, point to possibilities for future refinement. The development of a detailed computational model for lower limb lymphedema is not only scientifically valuable but also clinically relevant. Through refined simulations, clinicians may gain insights into patient-specific responses to treatment and adjust therapeutic strategies accordingly. In turn, this could enhance treatment outcomes and improve the quality of life for individuals living with this challenging condition.

Acknowledgements The project was supported financially by the Symphonies Project and the authors are very grateful to all the participants to this project for their helpful feedback during the numerous meetings. The authors would also like to thank Alexandra Vallet for the interesting scientific discussions around poroelasticity of soft tissues.

Author contributions Conceptualization contributed by Maha Reda, Stéphane Avril; methodology contributed by Maha Reda; formal analysis and investigation contributed by Maha Reda; writing—original draft preparation contributed by Maha Reda; writing—review and editing contributed by Stéphane Avril; funding acquisition contributed by Stéphane Avril; resources contributed by Stéphane Avril; supervision contributed by Stéphane Avril.

Funding The project was funded by BPI France.

Data availability No datasets were generated or analyzed during the current study.

Declarations

Conflict of interest The authors declare that they have no Conflict of interest related to this article.

References

Avril S, Bouten L, Dubuis L et al (2010) Mixed experimental and numerical approach for characterizing the biomechanical response of the human leg under elastic compression. J Biomech Eng 132:031006. https://doi.org/10.1115/1.4000967

Avril S, Badel P, Dubuis L et al (2012) Patient-specific modeling of leg compression in the treatment of venous deficiency. Springer, Berlin, pp 217–238. https://doi.org/10.1007/8415_2011_103

Baish JW, Padera TP, Munn LL (2022) The effects of gravity and compression on interstitial fluid transport in the lower limb. Sci Rep 12:4890. https://doi.org/10.1038/s41598-022-09028-9

Baxter LT, Jain RK (1989) Transport of fluid and macromolecules in tumors. i. role of interstitial pressure and convection. Microvasc Res 37(1):77–104. https://doi.org/10.1016/0026-2862(89)90074-5

Bertram CD (2020) Modelling secondary lymphatic valves with a flexible vessel wall: how geometry and material properties combine to provide function. Biomech Model Mechanobiol 19:2081–2098. https://doi.org/10.1007/s10237-020-01325-4

Bertram CD, Davis MJ (2023) An enhanced 3d model of intravascular lymphatic valves to assess leaflet apposition and transvalvular differences in wall distensibility. Biology 12:379. https://doi.org/10.3390/biology12030379

Biglia N, Librino A, Ottino MC et al (2015) Lower limb lymphedema and neurological complications after lymphadenectomy for gynecological cancer. Int J Gynecol Cancer 25:521–525. https://doi.org/10.1097/IGC.0000000000000341

Brace RA (1981) Progress toward resolving the controversy of positive vs. negative interstitial fluid pressure. Circ Res 49(2):281–297. https://doi.org/10.1161/01.RES.49.2.281

Brix B, Sery O, Onorato A et al (2021) Biology of lymphedema. Biology 10(4):261. https://doi.org/10.3390/biology10040261

Bunke N, Brown K, Bergan J (2009) Phlebolymphemeda: usually unrecognized, often poorly treated. Perspect Vasc Surg Endovasc Ther 21:65–68. https://doi.org/10.1177/1531003509337155

Cariati A, Piromalli E, Cariati P (2012) Effects of compression therapy and antibiotics on lymphatic flow and chronic venous leg ulceration. Arch Dermatol Res 304(6):497–498. https://doi.org/10.1007/s00403-012-1220-x

Chassagne F, Molimard J, Convert R et al (2016) Numerical approach for the assessment of pressure generated by elastic compression bandage. Ann Biomed Eng 44:3096–3108. https://doi.org/10.1007/s10439-016-1597-3

Chassagne F, Badel P, Molimard J (2019) Lower leg compression and its biomechanical effects on the soft tissues of the leg. Innovations and Emerging Technologies in Wound Care. pp 55–85. https://doi.org/10.1016/B978-0-12-815028-3.00004-3

Contarino C, Toro EF (2018) A one-dimensional mathematical model of collecting lymphatics coupled with an electro-fluid-mechanical contraction model and valve dynamics. Biomech Model Mechanobiol 17:1687–1714. https://doi.org/10.1007/s10237-018-1050-7

Dayan JH, Wiser I, Verma R et al (2020) Regional patterns of fluid and fat accumulation in patients with lower extremity lymphedema using magnetic resonance angiography. Plast Reconstr Surg 145:555–563. https://doi.org/10.1097/PRS.0000000000006520

Eymard N, Volpert V, Quere I et al (2017) A 2d computational model of lymphedema and of its management with compression device. Math Model Nat Phenomena 12:180–195. https://doi.org/10.1051/mmnp/201712511

Frauziols F, Molimard J, Navarro L et al (2015) Prediction of the biomechanical effects of compression therapy by finite element modeling and ultrasound elastography. IEEE Trans Biomed Eng 62:1011–1019. https://doi.org/10.1109/TBME.2014.2378553

Gaied I, Drapier S, Lun B (2006) Experimental assessment and analytical 2d predictions of the stocking pressures induced on a model leg by medical compressive stockings. J Biomech 39:3017–3025. https://doi.org/10.1016/j.jbiomech.2005.10.022

Gianesini S, Raffetto JD, Mosti G et al (2020) Volume control of the lower limb with graduated compression during different muscle pump activation conditions and the relation to limb circumference variation. J Vasc Surg Venous Lymphat Disord 8:814–820. https://doi.org/10.1016/j.jvsv.2019.12.073

Greiner A, Reiter N, Paulsen F et al (2021) Poro-viscoelastic effects during biomechanical testing of human brain tissue. Front Mech Eng 7:708350. https://doi.org/10.3389/fmech.2021.708350

Guyton AC (1965) Interstitial fluid pressure: Ii. pressure-volume curves of interstitial space. Circ Res 16(5):452–460. https://doi.org/10.1161/01.RES.16.5.452

Guyton AC, Granger HJ, Taylor AE (1971) Interstitial fluid pressure. Physiol Rev 51(3):527–563. https://doi.org/10.1152/physrev.1971.51.3.527

Heppell C, Richardson G, Roose T (2013) A model for fluid drainage by the lymphatic system. Bull Math Biol 75:49–81. https://doi.org/10.1007/s11538-012-9793-2

Heppell C, Roose T, Richardson G (2015) A model for interstitial drainage through a sliding lymphatic valve. Bull Math Biol 77:1101–1131. https://doi.org/10.1007/s11538-015-0078-4

Jamalian S, Jafarnejad M, Zawieja SD et al (2017) Demonstration and analysis of the suction effect for pumping lymph from tissue beds at subatmospheric pressure. Sci Rep 7:12080. https://doi.org/10.1038/s41598-017-11599-x

Jayathungage Don TD, Safaei S, Maso Talou GD et al (2024) Computational fluid dynamic modeling of the lymphatic system: a review of existing models and future directions. Biomech Model Mechanobiol 23(1):3–22. https://doi.org/10.1007/s10237-023-01780-9

Kaczmarek M, Olszewski WL, Nowak J et al (2015) The hydromechanics of edema fluid in lymphedematous lower limb during intermittent pneumatic compression. Lymphat Res Biol 13:260–267. https://doi.org/10.1089/lrb.2013.0047

Kedarasetti RT, Drew PJ, Costanzo F (2022) Arterial vasodilation drives convective fluid flow in the brain: a poroelastic model. Fluids Barriers CNS 19:34. https://doi.org/10.1186/s12987-022-00326-y

Koudehi GA, Delgado CAS, Impe MV et al (2023) Modelling lymph propulsion in a 3d model of murine collecting vessel with three lymphangions in series. Artery Res 29:101–120. https://doi.org/10.1007/s44200-023-00038-0

Koudehi GA, Delgado CAS, Impe MV et al (2023) Modelling lymph propulsion in a 3d model of murine collecting vessel with three lymphangions in series. Artery Res 29:101–120. https://doi.org/10.1007/s44200-023-00038-0

Lai WM, Mow VC (1980) Drag-induced compression of articular cartilage during a permeation experiment1. Biorheology 17(1–2):111–123. https://doi.org/10.3233/BIR-1980-171-213

Lu Q, Li Y, Chen TW et al (2014) Validity of soft-tissue thickness of calf measured using MRI for assessing unilateral lower extremity lymphoedema secondary to cervical and endometrial cancer treatments. Clin Radiol 69:1287–1294. https://doi.org/10.1016/j.crad.2014.08.011

Macdonald AJ, Arkill KP, Tabor GR et al (2008) Modeling flow in collecting lymphatic vessels: one-dimensional flow through a series of contractile elements. Am J Physiol Heart Circ Physiol 295:305–313. https://doi.org/10.1152/ajpheart.00004.2008.-The

Montalibet A, Rastel D, Chaigneau C et al (2020) Comparison between bioelectrical impedance spectroscopy measurements and water volume displacement of ankle oedema variations during the course of a day. Physiol Meas 41(8):085004. https://doi.org/10.1088/1361-6579/abaa57

Moore JE, Bertram CD (2018) Lymphatic system flows. Annu Rev Fluid Mech 50:459–482. https://doi.org/10.1146/annurev-fluid-122316-045259

Morgan PA, Franks PJ, Moffatt CJ (2005) Health-related quality of life with lymphoedema: a review of the literature. Int Wound J 2(1):47–62. https://doi.org/10.1111/j.1742-4801.2005.00066.x

Mosti G, Partsch H (2013) Bandages or double stockings for the initial therapy of venous oedema? A randomized, controlled pilot study. Eur J Vasc Endovasc Surg 46:142–148. https://doi.org/10.1016/j.ejvs.2013.04.015

Olszewski WL, Jain P, Ambujam G et al (2011) Tissue fluid pressure and flow during pneumatic compression in lymphedema of lower limbs. Lymphat Res Biol 9:77–83. https://doi.org/10.1089/lrb.2009.0025

Partsch B, Partsch H (2005) Calf compression pressure required to achieve venous closure from supine to standing positions. J Vasc Surg 42(4):734–738. https://doi.org/10.1016/j.jvs.2005.06.030

Partsch H (2012) Compression therapy: clinical and experimental evidence. Ann Vasc Dis 5:416–422. https://doi.org/10.3400/avd.ra.12.00068

Partsch H, Stout N, Forner-Cordero I et al (2010) Clinical trials needed to evaluate compression therapy in breast cancer related lymphedema (bcrl). Proposals from an expert group. Int Angiol J Int Union Angiol 29(5):442–453

Pflug JJ, Calnan JS (1971) The normal anatomy of the lymphatic system in the human leg. J British Surg 58:925–930. https://doi.org/10.1002/bjs.1800581216

Phillips JJ, Gordon SJ (2019) Intermittent pneumatic compression dosage for adults and children with lymphedema: a systematic review. Lymphat Res Biol 17:2–18. https://doi.org/10.1089/lrb.2018.0034

Reddy NP, Krouskop TA, Newell PH (1977) A computer model of the lymphatic system. Comput Biol Med 7(3):181–197. https://doi.org/10.1016/0010-4825(77)90023-3

Rohan CP, Badel P, Lun B et al (2013) Biomechanical response of varicose veins to elastic compression: a numerical study. J Biomech 46:599–603. https://doi.org/10.1016/j.jbiomech.2012.10.043

Rohan PY, Badel P, Lun B et al (2015) Prediction of the biomechanical effects of compression therapy on deep veins using finite element modelling. Ann Biomed Eng 43:314–324. https://doi.org/10.1007/s10439-014-1121-6

Schacht V, Luedemann W, Abels C et al (2009) Anatomy of the subcutaneous lymph vascular network of the human leg in relation to the great saphenous vein. Anat Rec 292:87–93. https://doi.org/10.1002/ar.20765

Shinaoka A, Koshimune S, Suami H et al (2020) Lower-limb lymphatic drainage pathways and lymph nodes: a ct lymphangiography cadaver study. Radiology 294:223–229. https://doi.org/10.1148/radiol.2019191169

Sowinski DR, McGarry MD, Houten EEV et al (2021) Poroelasticity as a model of soft tissue structure: Hydraulic permeability reconstruction for magnetic resonance elastography in silico. Front Phys 8:617582. https://doi.org/10.3389/fphy.2020.617582

Suehiro K, Morikage N, Murakami M et al (2013) Significance of ultrasound examination of skin and subcutaneous tissue in secondary lower extremity lymphedema. Ann Vasc Dis 6:180–188. https://doi.org/10.3400/avd.oa.12.00102

Swartz MA (2001) The physiology of the lymphatic system. Adv Drug Deliv Rev 50(1):3–20. https://doi.org/10.1016/S0169-409X(01)00150-8. (**transport and absorption of Drugs Via the Lymphatic System**)

Tassenoy A, Strijcker DD, Adriaenssens N et al (2016) The use of noninvasive imaging techniques in the assessment of secondary lymphedema tissue changes as part of staging lymphedema.

Lymphat Res Biol 14:127–133. https://doi.org/10.1089/lrb.2016.0011

Taylor AE (1981) Capillary fluid filtration. Starling forces and lymph flow. Circ Res 49(3):557–575. https://doi.org/10.1161/01.RES.49.3.557

Uzkeser H, Karatay S, Erdemci B et al (2015) Efficacy of manual lymphatic drainage and intermittent pneumatic compression pump use in the treatment of lymphedema after mastectomy: a randomized controlled trial. Breast Cancer 22:300–307. https://doi.org/10.1007/s12282-013-0481-3

Zaleska M, Olszewski WL, Durlik M (2014) The effectiveness of intermittent pneumatic compression in long-term therapy of lymphedema of lower limbs. Lymphat Res Biol 12:103–109. https://doi.org/10.1089/lrb.2013.0033

Zaleska M, Olszewski WL, Cakala M et al (2015) Intermittent pneumatic compression enhances formation of edema tissue fluid channels in lymphedema of lower limbs. Lymphat Res Biol 13:146–153. https://doi.org/10.1089/lrb.2014.0010